

Pore-Scale Characterization of Two-Phase Flow Using Integral Geometry

Zhishang Liu¹  · Anna Herring²  · Christoph Arns¹  · Steffen Berg³  · Ryan T. Armstrong¹ 

Received: 26 August 2016 / Accepted: 7 March 2017 / Published online: 23 March 2017
© Springer Science+Business Media Dordrecht 2017

Abstract The pore-scale morphological description of two-phase flow is fundamental to the understanding of relative permeability. In this effort, we visualize multiphase flow during core flooding experiments using X-ray microcomputed tomography. Resulting phase morphologies are quantified using Minkowski Functionals and relative permeability is measured using an image-based method where lattice Boltzmann simulations are conducted on connected phases from pore-scale images. A capillary drainage transform is also employed on the imaged rock structure, which provides reasonable results for image-based relative permeability measurements even though it provides pore-scale morphologies for the wetting phase that are not comparable to the experimental data. For the experimental data, there is a strong correlation between non-wetting phase Euler characteristic and relative permeability, whereas there is a weak correlation for the wetting phase topology. The relative permeability of some rock types is found to be more sensitive to topological changes than others, demonstrating the influence that phase connectivity has on two-phase flow. We demonstrate the influence that phase morphology has on relative permeability and provide insight into phase topological changes that occur during multiphase flow.

Keywords Minkowski functionals · Euler characteristic · X-ray microcomputed tomography · Capillary drainage transform · Maximum inscribed spheres · Relative permeability

1 Introduction

Two-phase flow in porous media is important in many scientific and industrial fields, including oil production, geothermal energy extraction and ground water flow in soil. The relative

✉ Ryan T. Armstrong
ryan.armstrong@unsw.edu.au

¹ School of Petroleum Engineering, University of New South Wales, Sydney, Australia

² Department of Applied Mathematics, Research School of Physics and Engineering, Australian National University, Canberra, Australia

³ Shell Global Solutions International B.V., Kesslerpark 1, 2288 GS Rijswijk, The Netherlands

permeability of the non-wetting phase (NWP) and wetting phase (WP) are regarded as the key parameters to predict reservoir production rates and estimate recovery factors (Dullien 2012; Lake 1989). Relative permeability is known to depend on rock wettability, flow boundary conditions, interfacial tension, displacement history, experimental techniques (steady state versus unsteady state) and pore space morphology (Berg et al. 2008). However, it is the underlying phase morphological characteristics that influence phase permeability and these characteristics for two-phase flow are still being discovered (Khayrat and Jenny 2016; Datta et al. 2014a, b; Schlüter et al. 2016). Our current formulations to model two-phase flow and empirical correlations for expressing relative permeability usually only consider phase saturation and disregard all other phase morphological characteristics (Dullien 2012). This approach implicitly assumes that phase saturation is sufficient for characterizing the complex phase morphologies that occur during multiphase flow.

Based on the Carman–Kozeny (CK) equation (Carman 1956), Corey first put forward the function of phase saturation and relative permeability (Corey 1954) and extended with Brooks and Corey (1964) to provide the Brooks–Corey correlation:

$$K_{ro}(S_w) = (1 - S_{wn})^{N_o} \tag{1}$$

$$K_{rw}(S_w) = K_{rw}^o S_{wn}^{N_w} \tag{2}$$

$$S_{wn} = S_{wn}(S_w) = \frac{S_w - S_{wi}}{1 - S_{wi} - S_{orw}} \tag{3}$$

where K_{ro} and K_{rw} are the NWP and WP relative permeabilities, S_w is WP saturation, S_{wn} is normalized WP saturation, S_{wi} is irreducible WP saturation, S_{orw} is residual NWP saturation, and N_o and N_w are empirical parameters. These empirical parameters do not have any physical meaning based on first principles and are only used for fitting purposes. However, the general trends for this correlation are understood, e.g., it is well known that as capillary number increases the Brook-Corey exponents (N_o and N_w) decrease and end-point relative permeability increase (Fulcher et al. 1985). However, an understanding of the underlying pore-scale physics for these trends is missing. Also, the actual description of the pore-scale phase morphologies is not unique, i.e., for a given phase saturation different phase topologies and resulting relative permeabilities can exist (Joekar-Niasar et al. 2008).

The Carman–Kozeny equation was modified by Alpak et al. (1999) to account for changes in phase saturation and interfacial area:

$$K_{rw} = S_w^3 \frac{\tau}{\tau_w} \frac{A_T^2}{(A_{ow} + A_{ws})^2} \tag{4}$$

$$K_{ro} = S_o^3 \frac{\tau}{\tau_o} \frac{A_T^2}{(A_{ow} + A_{os})^2} \tag{5}$$

where A_T is the total surface area of the solid, A_{ow} is the interfacial area of NWP and WP, A_{ws} is the interfacial area of WP and solid, A_{os} is the interfacial area of NWP and solid, τ is the tortuosity of pore space, τ_w is the tortuosity of wetting phase and τ_o is the tortuosity of non-wetting phase. This correlation is a physical-based model that provides more insight into fractional flow even though it is based on a simple extension of the bundle of capillary tubes model presented by Carman (1956). The model identifies the importance of phase saturation, surface area between phases, and the tortuosity of the path through which fluids flow. However, we require an approach with parameters that are easily measured at the pore scale and can be volume-averaged for macroscale relationships, i.e., the independent parameters for relative permeability need to be easily transferable between scales.

The Minkowski functionals (MFs) are unique measurements that provide a robust toolkit for characterizing the morphology of complex materials. The MFs measured at the pore scale can also be volume-averaged and thus provide macroscale parameters. The MFs can be used to uniquely describe the volume, surface area, mean curvature, and Euler characteristic of any 3D object (Schlüter et al. 2016). Hadwiger's theorem states that every motion-invariant, conditionally continuous and additive functional in 3D can be written as a linear combination of the 4 Minkowski functionals (Mecke and Arns 2005; Schlüter et al. 2016). Researchers have used the MFs to quantify the morphological properties of materials and/or phases in dissipative systems (Vogel et al. 2010; Schlüter et al. 2016). For porous media flow, apart from phase saturation and surface area, recent works have also related the Euler characteristic to absolute permeability and the percolation threshold for porous systems. Recent works have also shown that for simple 2D porous media, the Euler characteristic can be used to collapse absolute permeability data to a single curve (Scholz et al. 2012). In addition, new methods have been proposed for the characterization of pore-scale images by using persistence diagrams, which characterize the persistence of topological features and provide a means to measure percolation length scales (Robins et al. 2015). However, there is only limited work that characterizes the morphological characteristics of two-phase flow. Most of the recent works are related to the study of pore-scale trapping mechanisms (Herring et al. 2013, 2015), which have found that trapping is dependent on the initial NWP connectivity and not just phase saturation. Schlüter et al. (2016) examined the interrelationships between phase saturation, surface area, and Euler characteristic and used these measurements to characterize unique displacement types. In continuation of this work, Armstrong et al. (2016) demonstrated that the volume-averaged Euler number can be used to characterize flow regimes during immiscible displacement even though pore-scale topological changes of the flowing phases are continuously occurring and that rate effects due to these topological changes occur at constant phase saturation. These new studies raise many interesting questions regarding the relationship between average phase morphological properties, resulting macroscale flow properties, and how these parameters can be utilized within our current two-phase flow theories.

The aforementioned experiments provide unprecedented insights into pore-scale multi-phase flow properties. However, they are time-consuming for the systematic characterization of reservoir rock. An alternative approach is to simulate two-phase flow using digital rock images. This approach however also has its own inherent problems that concern the accurate characterization of boundary conditions, image segmentation error, and uncertainties in surface wettability (Blunt et al. 2013; Meakin and Tartakovsky 2009; Wildenschild and Sheppard 2012). One of the simplest modeling approaches is the capillary drainage transform, which is a morphological method used to simulate capillary-dominated drainage (Hilpert and Miller 2001). It has been evaluated that this method can capture bulk rock properties such as capillary pressure versus saturation functions (Shikhov and Arns 2015) and by extraction of the resulting phase arrangements followed by utilization of the Lattice Boltzmann method the effective permeability of a given phase can be estimated reasonably well in comparison with standard steady state relative permeability measurements (Hussain et al. 2014; Berg et al. 2016). The capillary drainage transform assumes capillary-dominated flow and complete surface wetting conditions, i.e. 0 degree contact angle and only allows for the evaluation of connected phase relative permeability through coupling with the Lattice Boltzmann method (Berg et al. 2016; Hussain et al. 2014). Neglecting the complicated influence of ganglion dynamics, and assuming capillary-dominated flow, the capillary drainage transform provides reasonable bulk measurements (Hussain et al. 2014; Berg et al. 2016; Shikhov and Arns 2015); however, the capillary drainage transform may estimate these bulk properties for the wrong reasons.

In other words, the capillary drainage transform predicts phase morphologies that provide bulk measurements similar to experimental results; however, a direct comparison between simulated and experimental pore-scale phase morphologies have not been conducted.

Another difficulty with the simulation of digital rock data is the uncertainty of representative boundary conditions and the implications that boundary conditions may have on fluid phase morphologies. Recently, [Cueto-Felgueroso and Juanes \(2016\)](#) demonstrated the difference between pressure-controlled and rate-controlled drainage experiments using a simple characterization of energy landscape approach. There they show that different boundary conditions can lead to different displacement signatures. However, the influence that boundary conditions have on the resulting pore-scale phase morphologies has yet to be elucidated. Also, when comparing experimental X-ray microtomography data to pore-scale simulations an additional level of difficulty arises. For the experiment, the boundary conditions are applied at the inlet and outlet of the flow cell, whereas for pore-scale simulations the boundary conditions are applied at the top and bottom of the image domain ([Porter et al. 2009](#)). Thus, the question as to what boundary condition is most appropriate remains an open question since we do not know what is occurring between the inlet and imaged region. At the pore-scale fluid/fluid displacement events occur in bursts, which have non-local effects ([Armstrong and Berg 2013](#); [Armstrong et al. 2015](#)). Such events outside of the imaged region will influence the boundary condition for the imaged domain.

Herein, we examine phase morphologies in distinctly different rock types and develop insight into how these parameters influence relative permeability. We then extend the study to test the capillary drainage transform method and evaluate the resulting simulated phase morphologies and relative permeabilities. Overall, we find that NWP connectivity characterized by Euler characteristic has a strong influence on NWP relative permeability, whereas WP Euler characteristic has a lesser influence on WP relative permeability than the case for NWP.

2 Materials and Methods

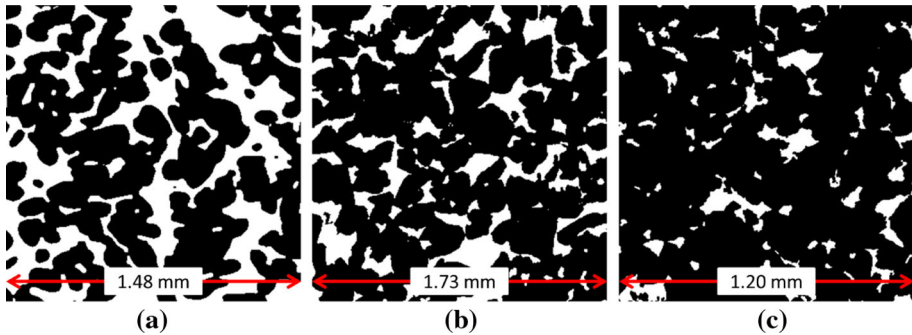
2.1 Microcomputed Tomography Imaging of Flow Experiments

We imaged fluid spatial arrangements during multiphase flow using two different experimental approaches. The first approach used synchrotron-based fast X-ray microcomputed tomography (micro-CT) to image fractional flow experiments in drainage mode, which we refer to as fractional flow drainage ([Schlüter et al. 2016](#)). The second experimental approach used a benchtop helical scanner from Australian National University to image quasi-static fluid arrangements during slow drainage, which we refer to as quasi-static primary drainage ([Herring et al. 2016](#)).

For the fractional flow drainage experiments, we used n-decane as the NWP and for the WP water doped with CsCl at a 1:6 weight ratio. Both phases were co-injected into a strongly water-wet sintered glass sample (Robuglass, diameter = 4.4 mm, length = 10 mm), see [Table 1](#) for petrophysical data. The flow cell was designed for dynamic experiments, the details of which can be found in a few of our recent publications ([Berg et al. 2013, 2014](#); [Armstrong et al. 2014a](#); [Rücker et al. 2015](#)). Fractional flow experiments started at $S_w = 1$, i.e. $F_w = 1$, and then by keeping the capillary number less than 10^{-5} and volumetric flow rate constant, we decreased the fractional flow F_w of the WP. Pressure was monitored until constant steady conditions were observed and then the fluid arrangements were imaged under dynamic flow conditions. The imaged fractional flow steps were $F_w = 0.8, 0.5$, and 0.2 . The

Table 1 Description of materials imaged in flow experiments, porosity is determined from segmented images

Rock type	Porosity (%)	Permeability (D)	Resolution (μm)	Image size (Voxel)
Robuglass	34.78	21.50	4.22	$1000 \times 1000 \times 572$
Bentheimer	24.10	4.25	4.95	$891 \times 891 \times 1440$
Leopard	15.56	0.21	3.44	$1265 \times 1265 \times 1800$

**Fig. 1** Samples of segmented images for different rock types (each size is 350×350 pixels, *black* is solid phase and *white* is void phase). **a** Robuglass. **b** Bentheimer. **c** Leopard

field of view for the experiment was approximately 4 mm in width and height, taken about 1 mm distance from the inlet to avoid the imaging of any boundary effect. The details of the beam line settings including energy, filters, camera, number of projections, angular steps, and optics were the same as that reported in our previous publications (Armstrong et al. 2014b). For the fractional flow drainage experiments, we tested only the Robuglass pore morphology.

For the quasi-static primary drainage experiments, we used ambient air as the NWP and brine (1:6 weight ratio of KI to degassed DI water) as the WP. The rock types tested are Bentheimer and Leopard sandstone. The details of the rock types tested are provided in Table 1. In Fig. 1, we display micro-CT images of each rock type; the Robuglass and Bentheimer samples are relatively homogeneous and well-sorted and the Leopard sandstone is more heterogeneous.

The quasi-static primary drainage experiments started at $S_w = 1$. WP was withdrawn from the sample at $18 \mu\text{l/h}$ (0.018 ml/h) via a syringe pump as NWP (ambient condition air) entered the core from the top of the core holder. A semi-permeable hydrophilic membrane was compressed to the bottom edge of the core to prevent NWP breakthrough from the core, which allowed for high NWP saturations to be achieved during drainage. The experimental setup has previously been described in Herring et al. (2016). All cores were 4.5 mm diameter and 10 mm long. The Leopard was imaged at 60 amp and 100 meV. The system was allowed 15 min to equilibrate after each pumping cycle prior to scanning; scans took 1 h and 40 min to acquire. Bentheimer was imaged at 65 amp and 100 meV and was allowed 5 min for equilibration, and each scan took 1 h and 21 min for each quasi-static 3D image. The Bentheimer sandstone sample was given a shorter equilibration time since it is a higher permeability rock. The equilibration times were determined from preliminary experiments where pressure transducer measurements were monitored. Images were taken about 1 mm from the inlet of the sample

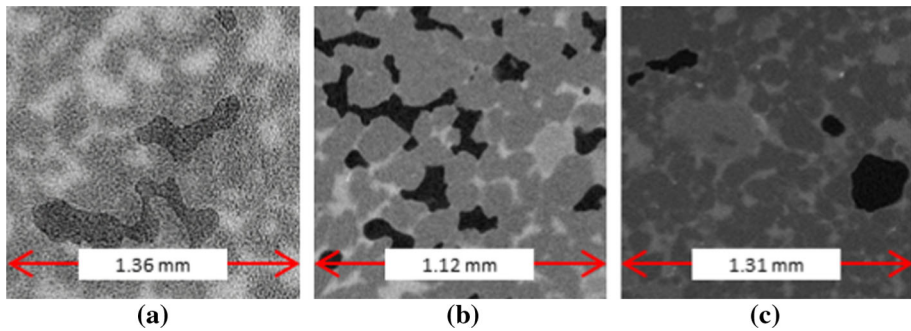


Fig. 2 Samples of reconstructed images for different rock types with fluids present in the pore space (WP is light gray while the NWP is dark gray). **a** Robuglass. **b** Bentheimer. **c** Leopard

for the quasi-static primary drainage experiments to avoid outlet boundary effects. Examples of the pore-scale images with fluids present in the pore space are provided in Fig. 2.

Initial dry images of each rock were collected and registered to the experimental images (fractional flow drainage and quasi-static primary drainage) using the methods presented by Latham et al. (2008). The registration step helps in segmenting the highly attenuating WP from the high attenuating solid grains. The images were segmented using gradient-based image segmentation techniques (Schlüter et al. 2014; Sheppard et al. 2004) and the identified WP and NWP were characterized using image quantification software that has been presented elsewhere (Arns et al. 2001, 2005b), which is briefly explained in the following subsections.

2.2 Capillary Drainage Transform

The capillary drainage transform mimics the invasion-percolation process of capillary-dominated flow in strongly water-wet porous media. The NWP is simulated to invade the pore space, which is completely saturated with WP. The maximum inscribed sphere of diameter D_s is related to the capillary pressure P_c by the following equation:

$$P_c = 4\sigma/D_s \quad (6)$$

where σ is interfacial tension and P_c is capillary pressure. To simulate capillary-dominated flow, according to the Young–Laplace equation, invasion into the pore space is determined by the pore size D_s that can be determined from the Euclidean distance map (EDM) of the pore space. A 6-neighborhood connectivity from the sample inlet is checked for each decremental decrease in D_s and disconnected regions are removed. In this way, we ensure phase connectivity and attempt to simulate primary drainage for connected phase flow. It is assumed that the wetting phase can escape through corner and film flow, which means trapped wetting phase will be reduced with increasing capillary pressure. Further details of the capillary drainage transform method are presented by others (Hilpert and Miller 2001; Silin and Patzek 2006; Arns et al. 2005c).

2.3 Minkowski Functionals and Phase Properties

The Minkowski functionals (MFs) can be used to describe the basic morphological properties of porous media. In 3D space, the Minkowski functionals involve four parameters that are defined as M_0 , M_1 , M_2 and M_3 , which are measurements of the volume, surface area, mean

Table 2 Minkowski functionals and WP/NWP characteristics

Minkowski functional	Corresponding characteristic
M_0	Volume
M_1	Surface area
M_2	Mean curvature
M_3	Euler characteristic

curvature and Euler characteristic of a given object, respectively (Arns et al. 2001). These four measurements uniquely define any object in 3D space. However, the magnitude of these values scales with system size and thus we normalize the absolute value by the total image volume. The normalized Minkowski functionals in voxel units are defined as:

$$m_{0x} = M_{0x} / V_{total} = V(x) / V_{total} \tag{7}$$

$$m_{1x} = M_{1x} / V_{total} = \frac{\int_{\delta x}^{\infty} ds}{6} / V_{total} = \frac{S(x)}{6} / V_{total} \tag{8}$$

$$m_{2x} = M_{2x} / V_{total} = \frac{\int_{\delta x}^{\infty} \left[\frac{1}{r_1} + \frac{1}{r_2} \right] ds}{3\pi} / V_{total} = \frac{C(x)}{3\pi} / V_{total} \tag{9}$$

$$m_{3x} = M_{3x} / V_{total} = \int_{\delta x}^{\infty} \frac{1}{r_1 r_2} ds / V_{total} = \chi(x) / V_{total} \tag{10}$$

where x can be for either the WP or NWP, V_{total} is the total sample volume, ds is an element of the surface, r_1 is the minimum curvature of ds , and r_2 is the maximum curvature of ds . Convex geometry contributes to positive mean curvature, which is the sign convention used in this work. The Minkowski functionals can be related to the intrinsic values including the volume $V(x)$, surface area $S(x)$, mean curvature $C(x)$ and Euler characteristic $\chi(x)$ by Eqs. 7–10. The Euler characteristic $\chi(x)$ can also be determined by the following equation:

$$\chi(x) = N - L + O \tag{11}$$

where N is the number of isolated object, L the number of redundant loops, and O is the number of cavities. A detailed illustration of the Euler characteristic for a few simple morphologies is available in our previous publication (Herring et al. 2013). Euler number describes the connectivity of a disordered material, redundant loops contribute to negative Euler numbers and isolated objects contribute to positive Euler number. The Minkowski functionals are calculated on the fluid phases of the segmented micro-CT images using the 4- and 6-neighborhoods for mean curvature and Euler characteristic, respectively. These values are calculated by a routine contained in the software package Morphy (Arns et al. 2001). Note that the underlying lattice resolution and solid phase segmentation is same for the simulation and experimental data sets. Therefore, any discretisation effects would have the same consequences for experiment and simulation (Table 2).

2.4 Effective Permeability and Relative Permeability Determination

To determine effective phase permeabilities, we simulate single phase flow in the connected regions (spanning clusters) of the pore-scale images using a 6-neighborhood connectivity. This approach has been presented in previous publications and was demonstrated to predict steady state relative permeability results reasonably well in comparison with laboratory mea-

sured relative permeability (Hussain et al. 2014; Berg et al. 2016). The relative permeability $K_{r,x}$ is calculated using the following equation

$$K_{r,x} = K_x / K_{\text{abs}}, (x = nw, w) \quad (12)$$

where K_{abs} is absolute permeability, K_x is effective permeability of phase x , and subscripts nw and w denote the NWP and WP, respectively. The absolute permeability is determined by single phase flow simulations on the entire void space, whereas the effective permeabilities are determined by single phase flow on the connected phase images collected from micro-CT flow experiments.

For measuring permeability, we employ the Lattice Boltzmann method (LBM) using D3Q19 (3D lattice with 19 possible momenta components) in the Morphy software package described by Arns et al. (2005a, b). The Bhatnager–Gross–Krook (BGK) model is used as the collision operator, and the boundary condition at the solid–fluid interfaces is no-flow condition that is realized using the bounce-back rule and a body force is the pressure gradient acting on the fluid (Arns et al. 2005a).

3 Results and Discussion

First, we compare the phase morphologies for the fractional flow drainage and quasi-static primary drainage experiments to results obtained from the capillary drainage transform. We then investigate the relationship between connected phase relative permeability and the 4 Minkowski functionals by measuring the correlation matrix of these parameters. The aim is to determine what phase morphology parameters have the largest influence on relative permeability by determining how well relative permeability correlates with each parameter. We identify the Euler number as a significant parameter for NWP relative permeability and investigate this relationship for all of the rock types tested.

3.1 Phase Morphologies During Multiphase Flow

We first present the phase morphology data for the fractional flow drainage and quasi-static primary drainage experiments with the simplest pore structures and compare these results to that predicted by the capillary drainage transform. Robuglass was selected as the fractional flow drainage sample and Bentheimer was the quasi-static primary drainage sample. Each Minkowski functional is presented as a function of WP saturation and both the micro-CT and capillary drainage transform data are compared. When the volume fraction of the pore space m_{0p} is calculated, m_{0x}/m_{0p} represents the saturation of phase x . The relative difference (Törnqvist et al. 1985) of phase x (error_x) between capillary drainage transform (CDT) and CT data is determined by Eq. 13:

$$\text{error}_x = \frac{\sum \text{abs}((f(\text{CT}_{xi}) - f(\text{CDT}_{xi}))/f(\text{CT}_{xi}))}{N} \quad (13)$$

where discrete CT and capillary drainage transform values are first interpolated into N data points at different WP saturation i , $f(\text{CT}_{xi})$ and $f(\text{CDT}_{xi})$ are the corresponding values of phase x at WP saturation i . The error is the average of the absolute difference between capillary drainage transform data and CT data at the same WP saturation divided by the CT data. When error = 0, it represents capillary drainage transform data and CT data completely overlap. When error is > 0, for example 1, it means capillary drainage transform data is one unit different from the CT data. Overall, according to the relative difference values, we find

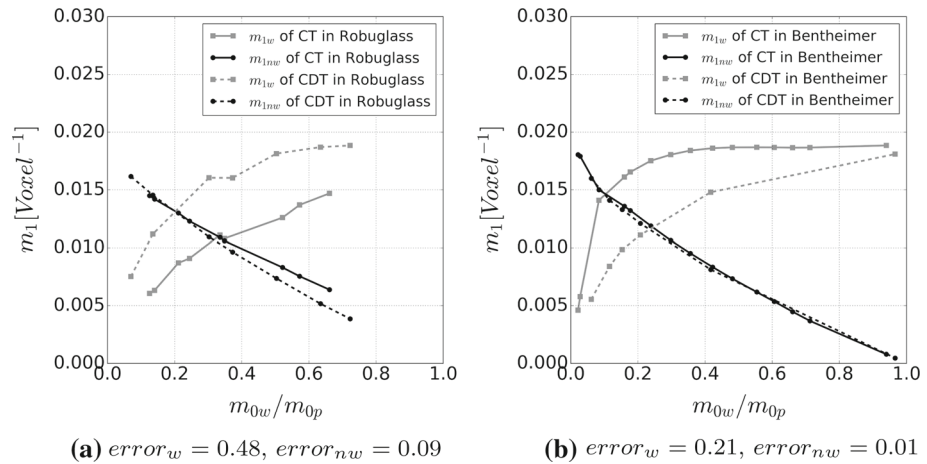


Fig. 3 Phase surface area at different wetting phase saturation for **a** fractional flow drainage and **b** quasi-static primary drainage experiments. *CT* microcomputed tomography data, *CDT* capillary drainage transform, *m1* surface area, m_{0w}/m_{0p} wetting phase saturation, *nw* non-wetting, and *w* wetting. The voxel length of Robuglass is 4.22 μm and Bentheimer is 4.95 μm

that the capillary drainage transform is able to predict the phase morphologies of the NWP for quasi-static primary drainage experiments and slightly less well the NWP morphologies for the fractional flow drainage experiments, whereas the WP morphologies are incorrect even though the trends seem reasonable. These results are explained further in the following subsections.

3.1.1 Phase Surface Area and Mean Curvature

In Fig. 3, we plot the phase surface area versus WP saturation. This is the total surface area of a given phase, which includes phase-phase and phase-solid interfacial areas. For example, for the NWP this is the sum of the NWP-solid and NWP-WP interfacial areas. We find that for the NWP in both the fractional flow drainage and quasi-static primary drainage experiments the capillary drainage transform does reasonably well at predicting the phase surface area. The relative difference between quasi-static primary drainage and capillary drainage transform data is 0.01, while the relative difference between fractional flow drainage and capillary drainage transform data is slightly higher at 0.09. However, for the WP surface area, the capillary drainage transform over predicts the surface area in the fractional flow drainage experiment ($error_w = 0.48$) and under predicts the surface area in quasi-static primary drainage experiment ($error_w = 0.21$) even though the overall trends are comparable.

For the quasi-static primary drainage data, the movement of the WP is mostly determined by capillary-dominated flow and in this case the capillary drainage transform does provide more accurate results for surface area than the fractional flow drainage data. The capillary drainage transform however still under predicts surface area, which could be because the transform (at the provided image resolution) does not capture the existence of WP in the crevices of the pore space as well as imaging of the experimental data does. For the fractional flow drainage data, the WP is flowing through larger connected pathways, which are less dominated by capillarity and of course the capillary drainage transform does not simulate this process. In this case, the capillary drainage transform provides surface area values that

are much higher than what is measured from the experimental data. However, for both the quasi-static primary drainage and fractional flow drainage data sets, the capillary drainage transform does capture the overall trends between surface areas and wetting phase saturation.

For both the quasi-static primary drainage and fractional flow drainage experiments the NWP surface area steadily increases with decreasing WP saturation to a final value that represents the phase surface area at connate water saturation, which corresponds to mostly NWP-Solid interfacial area. At low WP saturation, the interfaces for the WP are within the tightest of crevices of the pore space and thus the accurate measurement of interfacial area becomes a resolution problem for both the capillary drainage transform and experimental results. While the overall trend between surface area and saturation is captured with the capillary drainage transform the actual magnitude of the values, especially at low saturation, will result in error. Conversely, WP surface area increases with increasing WP saturation, which corresponds to a dominant increase in WP-solid interfacial area. In Fig. 3, the WP surface area approaches a maximum value at high WP saturation. This maximum value corresponds to the total WP-solid interfacial area plus a minimal amount of WP-NWP interfacial area. Overall, the capillary drainage transform performs reasonably well at predicting the phase surface area of the NWP for the tested strongly water-wet systems.

In Fig. 4, we plot phase mean curvature versus WP saturation, which includes contributions from both fluid/fluid and fluid/solid curvature. This means that the reported mean curvature value is not the average interfacial curvature of the fluid/fluid interface rather, it includes both fluid/fluid and fluid/solid curvature of the respective phase. Curvature data are even more susceptible to resolution error at low WP saturation since curvature is the second order derivative of the interface. In general, the Minkowski functionals are difficult to measure for the WP, which is an issue that has been discussed in detail by Arns et al. (2010). Overall, the general trends between curvature and saturation are comparable for the capillary drainage transform and experimental data; however, the actual magnitude of the curvatures resulting from these methods are not comparable. The accuracy of curvature measurements has been reviewed elsewhere (Armstrong et al. 2012). The capillary drainage transform simulates a

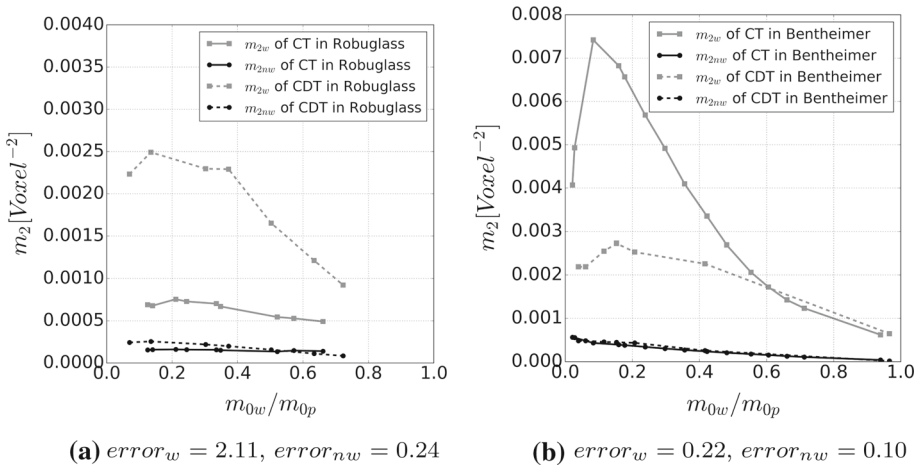


Fig. 4 Phase mean curvature at different wetting phase saturation for the fractional flow drainage (a) and quasi-static primary drainage (b) experiments. *CT* microcomputed tomography data, *CDT* capillary drainage transform, m_2 curvature, m_{0w}/m_{0p} wetting phase saturation, *nw* non-wetting, and *w* wetting. The voxel length of Robuglass is 4.22 μm and Bentheimer is 4.95 μm

higher WP mean curvature than the fractional flow drainage experiment ($error_w = 2.11$) and lower WP mean curvature than in quasi-static primary drainage experiments ($error_w = 0.22$), which is similar to the trends observed for the phase surface areas. For the quasi-static primary drainage experiments at low WP saturation, we measure high curvature as the WP retracts into the smallest crevices of the pore space. However, the capillary drainage transform does not seem to adequately capture these high curvature regions. Conversely, for the fractional flow drainage experiments due to connected phase flow and higher viscous forces (fractional flow drainage flow rates are 100x greater than the quasi-static drainage experiments), the WP interfaces are flatter and thus the measured mean curvature is lower and of course the capillary drainage transform does not capture the viscous effect and thus there is large error ($error_w = 2.11$). However, overall the NWP mean curvature values for the capillary drainage transform and experimental data are rather comparable with a measured relative difference of $error_{nw} = 0.10$ and $error_{nw} = 0.24$ for the quasi-static primary drainage and fractional flow drainage experiments, respectively (Fig. 4).

3.1.2 Phase Euler Number

In Fig. 5, we compare the phase Euler number versus WP saturation. We find that the capillary drainage transform results for NWP Euler characteristic are more comparable to the experimental data than the WP capillary drainage transform Euler characteristic results. For the NWP, we find a relative difference of $error_{nw} = 0.49$ and $error_{nw} = 0.89$ for the quasi-static primary drainage and fractional flow drainage experiments, respectively. Conversely for the WP, we measure much higher relative difference of $error_w = 1.79$ and $error_w = 5.85$ for the quasi-static primary drainage and fractional flow drainage experiments, respectively.

In Fig. 5a, the WP remains strongly connected in the fractional flow drainage experiment, i.e. m_{3w} remains less than zero, while the capillary drainage transform overtly over predicts positive m_{3w} values. The negative values in the fractional flow drainage experiment are likely caused by redundant loops of WP surrounding the grain surfaces, which is not entirely

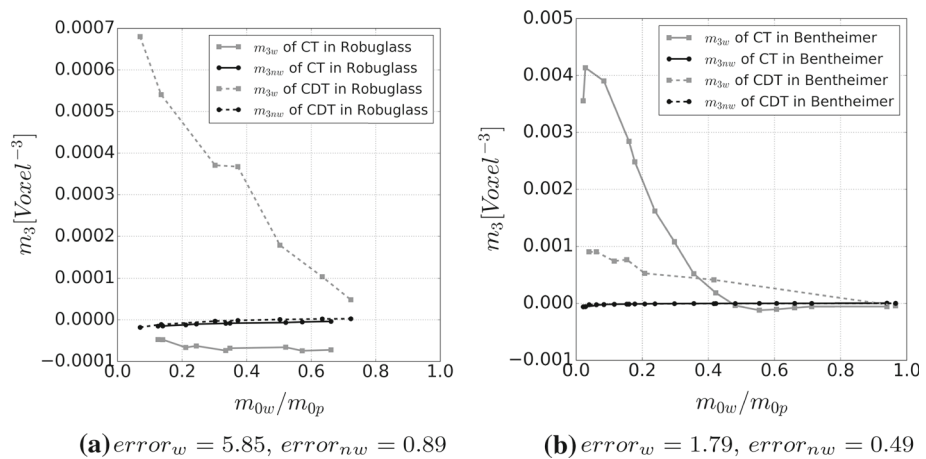


Fig. 5 Phase Euler number at different wetting phase saturation for the fractional flow drainage (a) and quasi-static primary drainage (b) experiments. CT microcomputed tomography data, CDT capillary drainage transform, m_3 Euler characteristic, m_{0w}/m_{0p} wetting phase saturation, nw non-wetting, and w wetting. The voxel length of Robuglass is $4.22 \mu\text{m}$ and Bentheimer is $4.95 \mu\text{m}$

captured with the capillary drainage transform. For this case, the capillary drainage transform forces disconnection of the WP, which clearly does not occur in the fractional flow drainage experiments. While this could be argued to be a resolution problem, it should be noted that both the capillary drainage transform and experimental data are conducted at the same image resolution. The capillary drainage transform results may be improved with grid refinement techniques; however, this would not be a 1 to 1 comparison with the micro-CT data since phase connectivity is also defined by the resolution at which it is imaged. For our comparison, the co-injection setup of the fractional flow drainage experiments retains WP connectivity, while the capillary drainage transform creates more disconnections when analyzed at the same resolution. The capillary drainage transform does better at predicting m_{3w} values for the quasi-static primary drainage experiments where co-injection does not occur, this may be because the boundary conditions are more comparable; however, the results are still unacceptable. For the quasi-static primary drainage experiments, a much larger degree of WP disconnection occurs in the experiments than that predicted by the capillary drainage transform. Once again, same as the other morphological descriptors, the capillary drainage transform only provides reasonable results for the NWP, and when it comes to phase topology the capillary drainage transform results are far worse than that obtained for the other Minkowski functionals.

3.2 Relationship Between Relative Permeability and Phase Morphology

We now explore the relationship between connected phase relative permeability and phase morphology. Previous work has shown that characteristic flow regimes provide unique phase topologies (Schlüter et al. 2016) and that average phase topologies can be used to characterize relative permeability (Armstrong et al. 2016). We also expand on previous work where connected phase relative permeabilities extracted from micro-CT flow experiments are shown to predict laboratory steady state relative permeability experiments (Berg et al. 2016). We first demonstrate how well the capillary drainage transform coupled with Lattice Boltzmann method is able to predict connected phase relative permeability even though, as previously shown, the phase morphologies for the WP are not comparable to the morphologies measured from experiments. From this analysis, we identify phase saturation as the most important parameter for relative permeability followed by Euler characteristic. We then further explore how phase morphology influences relative permeability by determining the correlation matrix for relative permeability and the MFs, which highlights the important role that NWP topology plays in NWP relative permeability. Lastly, we present trends between Euler number and relative permeability for 3 rock types and demonstrate that the relative permeability of some rock types are more sensitive to topological changes than others.

3.2.1 Relative Permeability Curves

In Fig. 6, we plot relative permeability versus saturation for the fractional flow drainage, quasi-static primary drainage and capillary drainage transform results. For each data set, we simulate single phase permeability for the phase morphology that is connected over the image domain. In this way, we measure the phase effective permeability (K_x is effective permeability of phase x) and relate this to relative permeability (K_{rx}) by normalizing the results by the simulated absolute permeability (K_{abs}), which was explained by Eq. 12. We find that, in accordance with previous relative permeability correlations, a strong power law-like relationship between phase saturation and relative permeability. We also find that the capillary drainage transform provides similar relative permeability results as the quasi-static primary drainage and fractional flow drainage experimental data. The relative difference

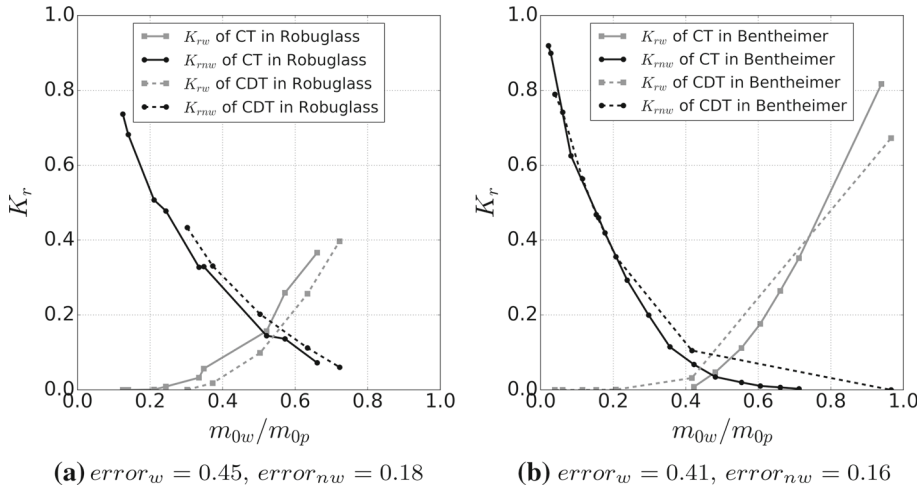


Fig. 6 Comparison of capillary drainage transform and CT relative permeability calculation at different m_{0w}/m_{0p} for the fractional flow drainage (a) and quasi-static primary drainage (b) experiments

for NWP relative permeability are $error_{nw} = 0.16$ and $error_{nw} = 0.18$ for the quasi-static primary drainage and fractional flow drainage experiments, respectively. Also, the relative difference for the WP relative permeability are only $error_w = 0.41$ and $error_w = 0.45$ for the quasi-static primary drainage and fractional flow drainage experiments, respectively.

Interestingly, even though the capillary drainage transform provides phase morphologies for the WP (and NWP in some cases) that are not comparable to the experimental micro-CT data the relative permeability results seem to be rather comparable. The WP relative permeability relative difference is rather low even though the relative differences for the WP phase morphologies are large, in particular the Euler number with a relative difference of 5.85 for the fractional flow drainage experiment. This suggests that phase saturation is the most important morphological characteristic for WP relative permeability, as previously assumed (Corey 1954; Carman 1956; Alpak et al. 1999). However, there are some differences in the relative permeability curves presented in Fig. 6, in particular the crossing-point of the curves are different, which determines the fractional flow of the phases. Also, the WP relative permeabilities still have relative differences greater than 0.40 and NWP relative permeabilities have arguably unreasonable results with relative differences greater than 0.15.

These findings also suggest that in multiphase flow modeling where after some tuning of the simulator an acceptable match with experimental data is obtained, this does not indicate that the underlying pore-scale fluid distributions are really correct. In other words, relative permeability is not a unique proof for correct pore-scale phase morphologies, which might have large implication in modeling processes where components are transferred between phases and/or other mass transfer processes are occurring.

3.2.2 Correlation Analysis

Herein we use the Pearson product-moment correlation to study the interrelationships between relative permeability and the four Minkowski functionals. The correlation matrix has been widely used to investigate the strength of association between multiple variables

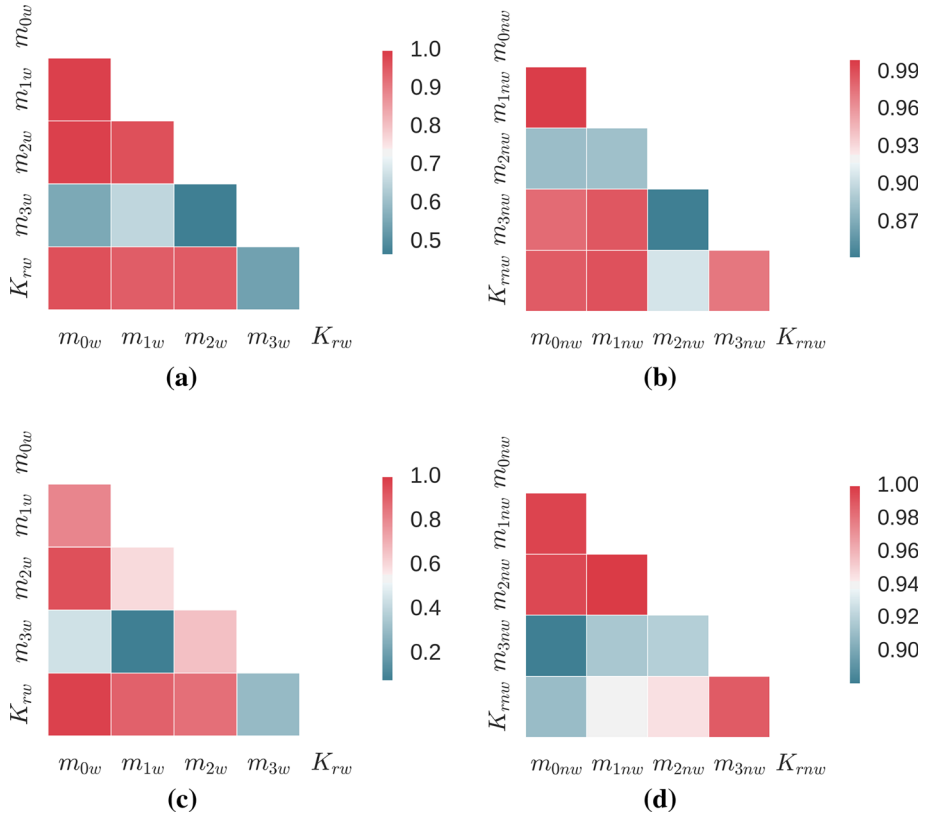


Fig. 7 Correlation matrix between relative permeability and Minkowski functionals. Note that each graph has a different color scale since the range of values are highly variable between figures. **a** WP of CT in Robuglass. **b** NWP of CT in Robuglass. **c** WP of CT in Bentheimer. **d** NWP of CT in Bentheimer

(Steiger 1980). The correlation coefficient can be calculated using Pearson correlation test method (Benesty et al. 2009) by Eq. 14:

$$r = \frac{N \sum xy - \sum x \sum y}{\sqrt{N \sum x^2 - (\sum x)^2} \sqrt{N \sum y^2 - (\sum y)^2}} \tag{14}$$

where r is the Pearson correlation coefficient, x and y are data sets and N is the number of values in each data set. The Pearson correlation coefficient ranges from 1 to -1 ; 1 is total positive correlation, 0 is no correlation, and -1 is total inverse correlation. A table containing the correlation coefficients between each MF, and relative permeability is shown in Fig. 7. The correlation matrix shows how strong the dependence is between $K_{rx}, m_{0x}, m_{1x}, m_{2x}$ and m_{3x} with respect to both WP and NWP. As previously mentioned the surface area and curvature of interfaces at low WP saturation are likely inaccurate due to resolution limitations. This is also the case for the WP topology. Since we cannot resolve thin films and/or WP in the smallest of crevices of the solid matrix and this influences the overall phase connectivity. However, the correlation is based on data from low, medium, and high WP saturations (more than 7 different saturations per sample) and any inaccuracies at low saturations (1-2 saturation points) will not influence the overall correlation.

In Fig. 7, we find a small correlation between K_{rw} and the Euler characteristic and a strong correlation between K_{rnw} and the Euler characteristic. As expected, there is also a strong correlation between phase volume (m_{0w} and m_{0nw}) and relative permeability for both sets of experimental data. However, there is a stronger correlation between saturation and relative permeability for WP than NWP. This explains some of the errors observed in the relative permeability curves when using the capillary drainage transform method. With the capillary drainage transform the phase saturations are correct, which results in reasonable relative permeability curves. For our data this means that a large relative error of 5.85 for WP topology provides only a smaller relative error of 0.45 in WP relative permeability. Whereas the capillary drainage transform captures NWP phase topology with a relative error of 0.89 and since topology is correlated with NWP relative permeability, this results in a more reasonable NWP relative permeability curve with relative error of 0.18.

We also find that the wettability of a given phase could be determined by using the correlation matrix by considering how strong the correlation is between relative permeability and Euler characteristic. Wettability can be determined by the m_{3w} and m_{3nw} rows of the correlation matrix. We find that for m_{3w} there is poor dependency on the other MFs, while for m_{3nw} there is a strong dependency on the other MFs. This occurs because the WP tends to swell and/or retract from the grain surfaces as phase saturation changes and this flow process maintains phase topology, whereas the NWP undergoes snap-off and/or pore-filling events that ultimately influence its topology as well as its curvature, area and saturation.

3.2.3 Euler Number Versus Relative Permeability

Following the correlation matrix, we find that K_{rnw} is strongly correlated with m_{3nw} and thus we examine this correlation in different rock types. The rock types tested are Robuglass, Bentheimer and Leopard sandstone. Coincidentally, we find that all m_{3nw} values lie between $[-0.00003, 0.00001]$ which are easily normalized into $[0, 1]$ by adding 0.00003 and divided by 0.00004 and thus providing the data presented in the Fig. 8. All data points are fitted to a power law relation using non-linear least squares method in `scipy.optimize.curve_fit` module in Python as $K_{rnw} = a \times m_{3nw}^b$, the parameters a and b for the tested rock types are listed in Table 3. As expected, for both the fractional flow drainage and quasi-static primary drainage experiments and for all rock types, the NWP relative permeability is strongly correlated with the NWP Euler characteristic.

Note that in Eq. 11, where the Euler characteristic is equal to the number of isolated objects minus the number of redundant loops plus the number of cavities. For the NWP, cavities are not physically realistic and thus the equation simplifies to $\chi_{nw} = N - L$ (isolated objects minus redundant loops), and then realizing that $\chi_{nw} < 1$ for the entire range of connected NWP relative permeability, which means that $L > N$. Therefore, effectively the relative permeability scales with the number of redundant loops. However, it depends on how these redundant loops are interconnected, which ultimately depends on the underlying pore morphology. For some rock types, the addition of redundant loops significantly influences the NWP relative permeability. Such is the case, for Robuglass and Bentheimer sandstone. Whereas for other rock types the addition of redundant loops has less effect on the NWP relative permeability, such is the case for Leopard sandstone. Ultimately, this effect is likely dependent on if the redundant loops are added in series or parallel and what pore network structure facilitate the additions of what type of loop.

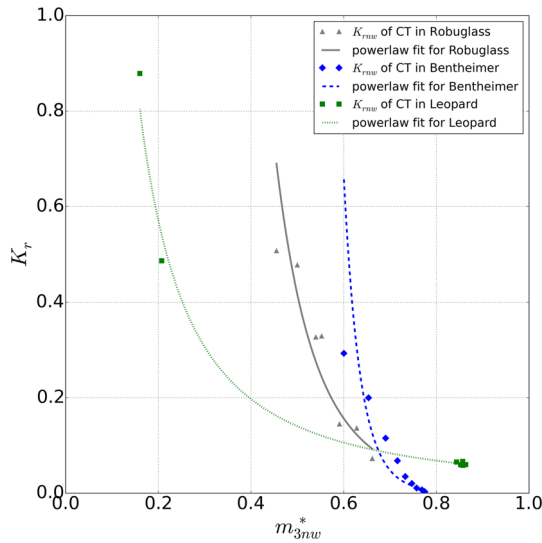


Fig. 8 K_{rnw} versus m_{3nw} of different rock types. Abbreviations; CT (microcomputed tomography data, m_{3nw} (non-wetting phase Euler characteristic) and nw (non-wetting phase)

Table 3 Parameters for the power law fit of different rock types

Rock type	Parameter a	Parameter b
Robuglass	-5.3612	0.0101
Bentheimer	-17.0791	0.0001
Leopard	-1.5346	0.0483

4 Conclusions

We conducted fractional flow drainage experiments in Robuglass and quasi-static primary drainage experiments in Bentheimer and Leopard sandstones and imaged the resulting phase topologies with X-ray microcomputed tomography. The distribution for NWP and WP are obtained and quantified using Minkowski Functionals and the relative permeabilities of both phases are calculated using lattice Boltzmann method. The main results are as follows:

- The capillary drainage transform fails to predict phase morphologies that are comparable to the experimental data even though the WP relative permeability compares well with the experimental data.
- The capillary drainage transform provides reasonable phase morphologies of the NWP and reasonably predicts NWP relative permeability.
- The Euler characteristic of the NWP is strongly correlated with NWP relative permeability, whereas the WP Euler characteristic is not correlated with WP relative permeability.
- Depending on the rock type, the addition of redundant loops can significantly influence relative permeability.

Apart from the findings, there are some shortcomings in this work:

- The lattice Boltzmann simulation approach is only capturing the connected pathway flow effective permeability, which does not capture the contribution of ganglion flow.

- The identification of boundary conditions for micro-CT flow experiments needs further studies. However, for the lower flow rate quasi-static experiments, the resulting NWP phase morphologies are similar to that predicted by the capillary drainage transform even though the boundary conditions are not consistent.
- The cross-relationship between MFs and relative permeability for different wettabilities requires further studies.
- The measurement of interfacial area and curvature at low WP saturations is likely inaccurate.

We provide the first look at how the MFs scale with relative permeability, provide insight into why previous works have been able to predict relative permeability using the capillary drainage transform method, and raise important questions regarding the influence of pore space morphologies and resulting phase topologies on relative permeability. For three different rock types, we find that NWP relative permeability is not only affected by NWP saturation, but is also influenced by NWP Euler characteristic. The main focus of this work is to demonstrate that relative permeability is not only a function of saturation but can be to a large extent parameterized with the 4 Minkowski functionals. Whether or not the parameterization by all 4 Minkowski functionals is complete, as Hadwiger's theorem would suggest, remains an open question. For future work, one prospect would be to employ this new characterization method to see if it can resolve relative permeability hysteresis.

Acknowledgements This research was undertaken with the assistance of resources provided at the NCI National Facility systems through the National Computational Merit Allocation Scheme. The Australian Government provided funding through an Australian Research Council (ARC) Discovery Project (DP160104995; RA, CHA) and an ARC Future Fellowship (FT120100216; CHA). We thank the anonymous reviewers for excellent comments that further strengthened this manuscript.

References

- Alpak, F.O., Lake, L.W., Embid, S.M.: In: SPE Annual Technical Conference and Exhibition, Society of Petroleum Engineers (1999)
- Armstrong, R.T., Berg, S.: Interfacial velocities and capillary pressure gradients during Haines jumps. *Phys. Rev. E* **88**(4), 043010 (2013)
- Armstrong, R.T., Evseev, N., Koroteev, D., Berg, S.: Modeling the velocity field during Haines jumps in porous media. *Adv. Water Resour.* **77**, 57–68 (2015)
- Armstrong, R.T., Georgiadis, A., Ott, H., Klemin, D., Berg, S.: Critical capillary number: desaturation studied with fast X-ray computed microtomography. *Geophys. Res. Lett.* **41**(1), 55–60 (2014a)
- Armstrong, R.T., Ott, H., Georgiadis, A., Rücker, M., Schwing, A., Berg, S.: Subsecond pore-scale displacement processes and relaxation dynamics in multiphase flow. *Water Resour. Res.* **50**(12), 9162–9176 (2014b)
- Armstrong, R.T., McClure, J.E., Berrill, M.A., Rücker, M., Schlüter, S., Berg, S.: Beyond Darcy's law: the role of phase topology and ganglion dynamics for two-fluid flow. *Phys. Rev. E* **94**(4), 043113 (2016)
- Armstrong, R.T., Porter, M.L., Wildenschild, D.: Linking pore-scale interfacial curvature to column-scale capillary pressure. *Adv. Water Resour.* **46**, 55–62 (2012)
- Arns, C., Bauget, F., Sakellariou, A., Senden, T., Sheppard, A., Sok, R., Ghous, A., Pinczewski, W., Knackstedt, M., Kelly, J., et al.: Digital core laboratory: petrophysical analysis from 3D imaging of reservoir core fragments. *Petrophysics* **46**(04), 260–277 (2005a)
- Arns, C.H., Bauget, F., Limaye, A., Sakellariou, A., Senden, T., Sheppard, A., Sok, R.M., Pinczewski, V., Bakke, S., Berge, L.L., et al.: Pore scale characterization of carbonates using X-ray microtomography. *SPE J.* **10**(04), 475–484 (2005b)
- Arns, C.H., Knackstedt, M.A., Martys, N.S.: Cross-property correlations and permeability estimation in sandstone. *Phys. Rev. E* **72**(4), 046304 (2005c)
- Arns, C., Knackstedt, M., Mecke, K.: 3D structural analysis: sensitivity of Minkowski functionals. *J. Microsc.* **240**(3), 181–196 (2010)

- Arns, C.H., Knackstedt, M.A., Pinczewski, W.V., Mecke, K.R.: Euler–Poincaré characteristics of classes of disordered media. *Phys. Rev. E* **63**(3), 031112 (2001)
- Benesty, J., Chen, J., Huang, Y., Cohen, I.: Pearson correlation coefficient. In: *Noise reduction in speech processing*, pp. 1–4. Springer, Berlin Heidelberg (2009)
- Berg, S., Armstrong, R., Ott, H., Georgiadis, A., Klapp, S., Schwing, A., Neiteler, R., Brussee, N., Makurat, A., Leu, L., et al.: Multiphase flow in porous rock imaged under dynamic flow conditions with fast X-ray computed microtomography. *Petrophysics* **55**(04), 304–312 (2014)
- Berg, S., Cense, A., Hofman, J., Smits, R.: Two-phase flow in porous media with slip boundary condition. *Transp. Porous Media* **74**(3), 275–292 (2008)
- Berg, S., Ott, H., Klapp, S.A., Schwing, A., Neiteler, R., Brussee, N., Makurat, A., Leu, L., Enzmann, F., Schwarz, J.O., et al.: Real-time 3D imaging of Haines jumps in porous media flow. *Proc. Natl. Acad. Sci.* **110**(10), 3755–3759 (2013)
- Berg, S., Rücker, M., Ott, H., Georgiadis, A., van der Linde, H., Enzmann, F., Kersten, M., Armstrong, R., de With, S., Becker, J., et al.: Connected pathway relative permeability from pore-scale imaging of imbibition. *Adv. Water Resour.* **90**, 24–35 (2016)
- Blunt, M.J., Bijeljic, B., Dong, H., Gharbi, O., Iglauer, S., Mostaghimi, P., Paluszny, A., Pentland, C.: Pore-scale imaging and modelling. *Adv. Water Resour.* **51**, 197–216 (2013)
- Brooks, R.H., Corey, A.T.: Hydraulic properties of porous media and their relation to drainage design. *Trans. ASAE* **7**(1), 26–0028 (1964)
- Carman, P.C.: *Flow of Gases Through Porous Media*. Academic Press, New York (1956)
- Corey, A.T.: The interrelation between gas and oil relative permeabilities. *Prod. Mon.* **19**(1), 38–41 (1954)
- Cueto-Felgueroso, L., Juanes, R.: A discrete-domain description of multiphase flow in porous media: rugged energy landscapes and the origin of hysteresis. *Geophys. Res. Lett.* **43**, 1615–1622 (2016)
- Datta, S.S., Dupin, J.B., Weitz, D.A.: Fluid breakup during simultaneous two-phase flow through a three-dimensional porous medium. *Phys. Fluids* **26**(6), 062004 (2014a)
- Datta, S.S., Ramakrishnan, T., Weitz, D.A.: Mobilization of a trapped non-wetting fluid from a three-dimensional porous medium. *Phys. Fluids* **26**(2), 022002 (2014b)
- Dullien, F.A.: *Porous Media: Fluid Transport and Pore Structure*. Academic Press, San Diego (2012)
- Fulcher Jr., R.A., Ertekin, T., Stahl, C., et al.: Effect of capillary number and its constituents on two-phase relative permeability curves. *J. Pet. Technol.* **37**(02), 249–260 (1985)
- Herring, A.L., Andersson, L., Schlüter, S., Sheppard, A., Wildenschild, D.: Efficiently engineering pore-scale processes: the role of force dominance and topology during nonwetting phase trapping in porous media. *Adv. Water Resour.* **79**, 91–102 (2015)
- Herring, A.L., Harper, E.J., Andersson, L., Sheppard, A., Bay, B.K., Wildenschild, D.: Effect of fluid topology on residual nonwetting phase trapping: implications for geologic CO₂ sequestration. *Adv. Water Resour.* **62**, 47–58 (2013)
- Herring, A.L., Sheppard, A., Andersson, L., Wildenschild, D.: Impact of wettability alteration on 3D nonwetting phase trapping and transport. *Int. J. Greenh. Gas Control* **46**, 175–186 (2016)
- Hilpert, M., Miller, C.T.: Pore-morphology-based simulation of drainage in totally wetting porous media. *Adv. Water Resour.* **24**(3), 243–255 (2001)
- Hussain, F., Pinczewski, W.V., Cinar, Y., Arns, C., Turner, M.: Computation of relative permeability from imaged fluid distributions at the pore scale. *Transp. Porous Media* **104**(1), 91–107 (2014)
- Joekar-Niasar, V., Hassanizadeh, S., Leijne, A.: Insights into the relationships among capillary pressure, saturation, interfacial area and relative permeability using pore-network modeling. *Transp. Porous Media* **74**(2), 201–219 (2008)
- Khayrat, K., Jenny, P.: Subphase approach to model hysteretic two-phase flow in porous media. *Transp. Porous Media* **111**(1), 1–25 (2016)
- Lake, L.: *Enhanced Oil Recovery*. Prentice Hall Inc., Old Tappan (1989)
- Latham, S., Varslot, T., Sheppard, A., et al.: Image registration: enhancing and calibrating X-ray micro-CT imaging. In: *Proceedings of the Society Core Analysts*, Abu Dhabi, UAE (2008)
- Meakin, P., Tartakovsky, A.M.: Modeling and simulation of pore-scale multiphase fluid flow and reactive transport in fractured and porous media. *Rev. Geophys.* **47**(3), RG3002 (2009)
- Mecke, K., Arns, C.: Fluids in porous media: a morphometric approach. *J. Phys. Condens. Matter* **17**(9), S503 (2005)
- Porter, M.L., Schaap, M.G., Wildenschild, D.: Lattice-Boltzmann simulations of the capillary pressure-saturation-interfacial area relationship for porous media. *Adv. Water Resour.* **32**(11), 1632–1640 (2009)
- Robins, V., Saadatfar, M., Delgado-Friedrichs, O., Sheppard, A.P.: Percolating length scales from topological persistence analysis of micro-CT images of porous materials. *Water Resour. Res.* **52**(1), 315–329 (2016)

- Rücker, M., Berg, S., Armstrong, R., Georgiadis, A., Ott, H., Schwing, A., Neiteler, R., Brussee, N., Makurat, A., Leu, L., et al.: From connected pathway flow to ganglion dynamics. *Geophys. Res. Lett.* **42**(10), 3888–3894 (2015)
- Schlüter, S., Berg, S., Rücker, M., Armstrong, R., Vogel, H.J., Hilfer, R., Wildenschild, D.: Pore-scale displacement mechanisms as a source of hysteresis for two-phase flow in porous media. *Water Resour. Res.* **52**(3), 2194–2205 (2016)
- Schlüter, S., Sheppard, A., Brown, K., Wildenschild, D.: Image processing of multiphase images obtained via X-ray microtomography: a review. *Water Resour. Res.* **50**(4), 3615–3639 (2014)
- Scholz, C., Wirner, F., Götz, J., Råde, U., Schröder-Turk, G.E., Mecke, K., Bechinger, C.: Permeability of porous materials determined from the Euler characteristic. *Phys. Rev. Lett.* **109**(26), 264504 (2012)
- Sheppard, A.P., Sok, R.M., Averdunk, H.: Techniques for image enhancement and segmentation of tomographic images of porous materials. *Phys. A Stat. Mech. Appl.* **339**(1), 145–151 (2004)
- Shikhov, I., Arns, C.H.: Evaluation of capillary pressure methods via digital rock simulations. *Transp. Porous Media* **107**(2), 623–640 (2015)
- Silin, D., Patzek, T.: Pore space morphology analysis using maximal inscribed spheres. *Phys. A Stat. Mech. Appl.* **371**(2), 336–360 (2006)
- Steiger, J.H.: Tests for comparing elements of a correlation matrix. *Psychol. Bull.* **87**(2), 245 (1980)
- Törnqvist, L., Vartia, P., Vartia, Y.O.: How should relative changes be measured? *Am. Stat.* **39**(1), 43–46 (1985)
- Vogel, H.J., Weller, U., Schlüter, S.: Quantification of soil structure based on Minkowski functions. *Comput. Geosci.* **36**(10), 1236–1245 (2010)
- Wildenschild, D., Sheppard, A.P.: X-ray imaging and analysis techniques for quantifying pore-scale structure and processes in subsurface porous medium systems. *Adv. Water Resour.* **51**(2013), 217–246 (2012)